RSC Advances

PAPER

View Article Online
View Journal | View Issue

Cite this: *RSC Adv.*, 2022, **12**, 546

Oxygen and nitrogen enriched pectin-derived micro-meso porous carbon for CO_2 uptake

Milad Vafaeinia,[a] Mobin Safarzadeh Khosrowshahi,[a] Hossein Mashhadimoslem,[b] Hosein Banna Motejadded Emrooz *[a] and Ahad Ghaemi[a]

Oxygen and nitrogen enriched micro–meso porous carbon powders have been prepared from pectin and melamine as oxygen and nitrogen containing organic precursors, respectively. The synthesis process has been performed following a solvothermal approach in an alkaline solution during which Pluronic F127 was added to the solution as the soft template. Following the solvothermal treatment, the carbonization process has been performed at 700, 850 and 950 °C. The synthesized porous carbons have been characterized by X-ray diffraction (XRD), Raman spectroscopy, X-ray photoelectron spectroscopy (XPS), field emission scanning electron microscopy (FESEM), transmission electron microscopy (TEM), nitrogen adsorption–desorption isotherms and Fourier transform infrared spectroscopy (FTIR). The surface area of 499.5 $m^2\ g^{-1}$, total pore volume of 0.35 $cm^3\ g^{-1}$, and a high nitrogen and oxygen content of 9.3 and 29.1 wt% are displayed for the fine sample. The optimal porous carbon had CO_2 adsorption of up to 3.1 mmol g^{-1} at 273 K at 1 bar owing to abundant basic nitrogen-containing functionalities and the valuable micro–meso porous structure. Despite the absence of any reagent and also having a relatively moderate specific surface area, compared to similar materials, a very high ratio of adsorption capacity to specific surface area (6.2 μmol m^{-2}) was observed. The Elovich kinetic model was found to be the best and the physisorption process was reported.

Received 16th November 2021
Accepted 14th December 2021

DOI: 10.1039/d1ra08407k

rsc.li/rsc-advances

1. Introduction

Climate change is one of the most serious dangers to the environment, and the prominent cause is greenhouse gas (GHG) emissions. Among released GHGs, carbon dioxide (CO_2) represents the largest portion.[1] CO_2 carries out a significant role in global warming, and the concentration of this gas has risen steadily from around 325 ppm in 1967 to around 409 ppm (2017) and is expected to reach 570 ppm by the year 2100. As a result, the Earth's surface temperature will rise, resulting in some issues such as ocean acidification, health consequences, and so on.[2] To reduce CO_2 concentrations in the atmosphere, it is critical to develop carbon capture and storage (CCS) technologies.[3] Post-combustion, pre-combustion, and oxyfuel combustion capture are the three main forms of CCS. Post-combustion capture is the most commonly deployed CO_2 adsorption technique due to its simplicity and ease of fitting in existing coal-fired power plants.[4] Membrane isolation and cryogenic separation are other methods.[5,6] The gas–solid adsorption process is a low-cost energy method and solid adsorbents provide advantages such as high adsorption capacity, quick recovery, high uptake efficiency in humid situations, easy handling, and material stability.[7]

For CO_2 adsorption, solid porous materials such as zeolites,[8] metal–organic frameworks (MOFs),[9] and porous carbons,[10] are available. In these materials, there is no electron transfer between CO_2, and the adsorbent and molecules are preferentially adsorbed onto the surface of adsorbents.[11] Owing to their high CO_2 capture, zeolites are widely regarded as the main materials for CO_2 adsorption applications.[12] In a previous study, the H-ZSM-5 demonstrated CO_2 adsorption of 2.6 mmol g^{-1} at 273 K, at 1 bar under flue gas conditions.[13] MOFs are widely used as adsorbents due to their readily tunable pore geometry and surface properties. The ultramicroporous MOF (copper MOF) possesses a specific surface area of 945 $m^2\ g^{-1}$, showing CO_2 adsorption of 3.5 mmol g^{-1} at ambient temperature and pressure.[14] Using zeolites has several drawbacks: (1) producing defect-free zeolite crystals may be difficult, time-consuming, and expensive (2) zeolite shapes and compositions are restricted, and (3) expensive surface chemistries are frequently required to enhance adhesion to polymer matrices.[15] Also, MOFs have problems such as sensitivity to moisture, costly and difficult synthesis.[16] Due to their high thermal and chemical stability, high surface area, low cost, the low energy requirement for regeneration, surface modification, and tunable porous structure, porous carbons are considered the most promising CO_2 uptake candidates among these adsorbents.[17]

[a]*Nanotechnology Department, School of Advanced Technologies, Iran University of Science and Technology (IUST), Narmak, 16846, Tehran, Iran. E-mail: motejadded@iust.ac.ir*

[b]*School of Chemical, Petroleum and Gas Engineering, Iran University of Science and Technology (IUST), Narmak, 16846, Tehran, Iran*

The presence of heteroatoms and micropores in solid adsorbents improves material performance. The incorporation of heteroatoms into porous carbons is one of the most successful and popular strategies for improving CO_2 capture in carbon-based materials. When compared with non-doped carbon materials, heteroatoms can improve the electronegativity of porous carbons, resulting in better CO_2 capture.[17] Nitrogen (N)[18] and oxygen (O)[19] are the most common nonmetallic heteroatoms substituted in porous carbon materials. N-doped porous carbons have been developed to be utilized as CO_2 adsorbents due to the broad range of nitrogen sources. Nitrogen-containing groups, also including Lewis bases, are known to be active sites for acidic CO_2 binding.[20–22] Many research has been published on the effect of oxygen-containing groups on CO_2 adsorption. A study by Dawei *et al.* detected the interactions between CO_2 and oxygen functional groups were stronger than the interactions between CO_2 and carbon surface. This point shows a positive effect of oxygen functional groups on CO_2 uptake.[23] Also, results show that heteroatom groups (such as C–O and C=O) may provide more active sites for nitrogen functional groups entry.[24] Furthermore, at 273 K and 1 bar, micropores smaller than 0.8 nm were suggested to be beneficial for CO_2 adsorption, and molecules are trapped in the narrow micropores.[25]

The choice of precursors is important for the production of porous carbons. Precursors can be typically divided into two specific categories: natural and synthetic. Through various synthesis methods, porous carbons are traditionally obtained by pyrolysis of a variety of C-rich materials as precursors, which can be synthetic (formaldehyde,[26] resorcinol,[27] and thiourea[28]) or natural (biomass, cheap agricultural, and materials with known chemical composition) such as pine cone,[29] chitosan,[21] and poplar wood.[30] Pectin is a low-cost natural polysaccharide and contains a linked α-D-galacturonic acid backbone with many hydroxyl and carboxyl groups. It is usually recognized in the biomedical and food markets and is easy can be extracted from the citrus pomace.[31] Pectin can be produced in a gel-like structure, and this gel might provide access to novel carbonaceous materials with unique porosity properties.[32] Pectin has been effectively used as a functional biopolymer to create N/O co-doped 3D carbon architecture with hierarchical pores for supercapacitor by Zhou *et al.*[33] As well as Zhang *et al.* using pectin as the porous carbon precursor, an adsorbent for methylene blue was gained.[31] Further, Yuanyuan *et al.* synthesized pectin-derived N, S-enriched carbon to enhance the charge transfer and oxygen reduction reaction (ORR) electrocatalysts activity.[34] According to the instances mentioned above, in our research, for the first time, pectin-based porous carbon is investigated for CO_2 uptake.

In this work, porous carbons with a high percentage of oxygen and nitrogen were synthesized using pectin and melamine as carbon, oxygen, and nitrogen precursors. Moreover, Pluronic F127 was used as a soft template. Pyrolysis was performed at 700, 850, and 950 °C, and the obtained samples were characterized by field emission scanning (FESEM) and transmission electron microscopy (TEM), Raman, Fourier-transform infrared (FTIR) and X-ray photoelectron spectroscopy (XPS), X-ray diffraction (XRD), thermogravimetry-differential thermal analysis (DTA-TG) and N_2 adsorption–desorption analysis. After characterization and determination of the best synthesized porous carbon, it was applied as the sorbent for CO_2 uptake. The results show that the optimal porous carbon has a high CO_2 adsorption capacity of 3.1 mmol g^{-1} at 1 bar, 273 K. The physisorption adsorption is derived from thermodynamic and kinetic analysis at different temperatures under various pressures. Eventually, a parameter called the amount of adsorption to the specific surface was introduced and the present synthesized porous carbon was compared with other developed porous carbons.

2. Experimental

2.1. Materials

Pectin was purchased ready made from a local confectionary market (Tehran, Iran) and melamine from Merck Company (Munich, Germany). Pluronic F127 was purchased from Sigma-Aldrich Company (Munich, Germany). Ammonia solution (25%) was purchased from Dr Mojallali™ Company (Tehran, Iran). All chemicals were analytical grade and utilized without additional purification as received.

2.2. Synthesis

To synthesize porous carbon, 1 g of melamine, 2 g of pectin, and 1 g of Pluronic F127 as template were added to 90 cm^3 of distilled water and 30 cm^3 of 25% ammonia at 343 K and stirred until full dissolution. The prepared clear solution was transferred to a reflux system and stirred for another 1 h at 363 K. Then, during normal cooling to the ambient temperature, a gel-like material was formed. The obtained gel was freeze-dried overnight at a temperature of −80 °C during which a foam-like structure was formed. The prepared foam was labeled as fmp. A similar foam was prepared without the addition of Pluronic F127 and labeled as mp. Then the foams were pyrolyzed under argon atmosphere in a tube furnace at 700, 850, and 950 °C. The obtained samples were labeled as mp*x* and fmp*x* where *x* represents the pyrolysis temperatures.

2.3. Characterization

Micromeritics ASAP2020 (US) adsorption analyzers was employed to measure the N_2 adsorption–desorption isotherms at 77 K. Before performing the adsorption–desorption analyses, samples were degassed under dynamic vacuum conditions to constant weight at a temperature of 393 K for 2 h. Raman spectroscopy was conducted on a Takram micro-Raman spectrometer (Teksan™, Iran). FTIR spectroscopy was accomplished on a PerkinElmer Spectrometer in the range of 500–4000 cm^{-1} with KBr pallets. X-ray photoelectron spectroscopy (XPS) measurements were carried out on an Al Kα source (XPS Spectrometer Kratos AXIS Supra). Transmission electron microscope (TEM) using Philips EM208S 100 kV. Thermogravimetric analyses (TG) in argon and air atmosphere were conducted on a Q600 (US) TA. Field emission scanning electron microscopy (FESEM) was observed on a Nanosem-450 microscope. Low-

pressure CO_2 adsorption isotherms of the synthesized porous carbon were measured at 273 K on an ASAP 2020 (US) Micromeritics at 0–1 bar.

2.4. Adsorption experimental procedure

A fixed bed adsorption reactor was used to evaluate the CO_2 adsorption–desorption performance of the synthesized porous carbon adsorbent, as shown in Fig. 1. In the research, pure CO_2 was used as a feed to evaluate the porous carbon surface's adsorption capacity. In the fully sealed cylindrical reactor, 0.5 g of porous carbon synthesized was loaded. Experiments were carried out for 90 minutes under 1 bar pressure at temperatures of (273, 298, 308, and 318 K). Thermodynamic parameters were investigated in temperature ranges from 298 to 328 K at 6 bar.

Because of the mixing tank in the route, the CO_2 pressure and temperature were stabilized, and the stable gas was then given to the adsorbent reactor. An electrical heat tracing provides heat to the reactor, and the computer records temperature and pressure variations in CO_2 in real time.

3. Results and discussions

3.1. Morphologic and characterization analysis

Fig. 2 shows % TG (Thermo Gravimetric) curves of samples in an argon atmosphere to follow the mass and structural changes of the foams synthesized with and without F127. The mechanism and temperatures of the reaction may be established according to this analysis, which exposes vital data regarding the decomposition behavior that happens as the temperature rises. The TG curves of both materials indicated 10–15% mass loss at 100–200 °C owing to the elimination of physically adsorbed water molecules.[35] For fmp and mp in the TG diagram, a weight loss zone occurred in the temperature range of 250 °C to 350 °C which is related to the decomposition of the

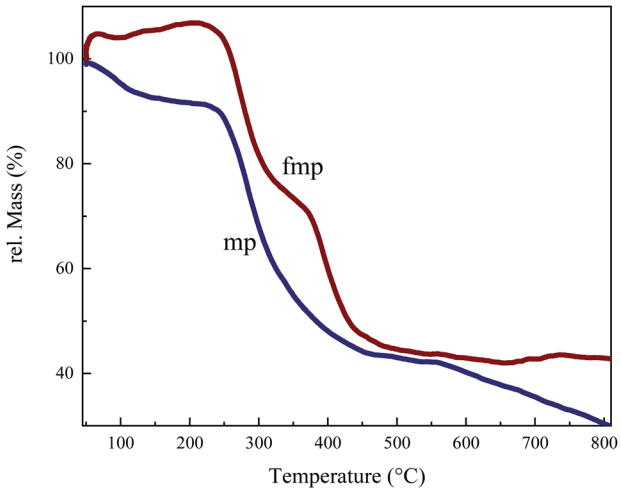

Fig. 2 Thermogravimetric results of fmp and mp under argon atmosphere.

polymerization resulting in the emission of CO_2 and H_2O. The fmp has a rapid weight loss in the range of 350 °C to 450 °C, which is due to the removal of the F127 from the structure. Continued weight loss in both samples is due to the carbonization of the samples. After 450 °C, fmp does not decrease weight, indicating that the carbon matrix is formed at this temperature.[36–38]

Fig. 3 depicts the structure, crystallinity, and textural characteristics of the pyrolyzed samples. The crystal structure of the materials was examined using XRD patterns. The production of turbostratic carbons with structural ordering intermediate between amorphous carbon and crystalline graphite is readily seen in X-ray diffraction patterns Fig. 3(a). Two broad diffraction peaks centered at around 2theta of 23.6° and 43.7° for

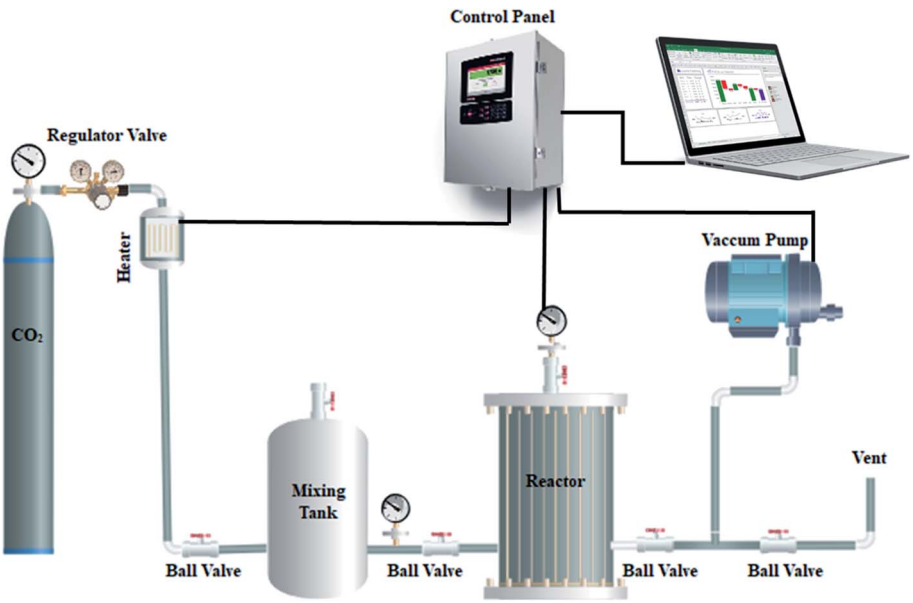

Fig. 1 Schema of experimental CO_2 adsorption set up.

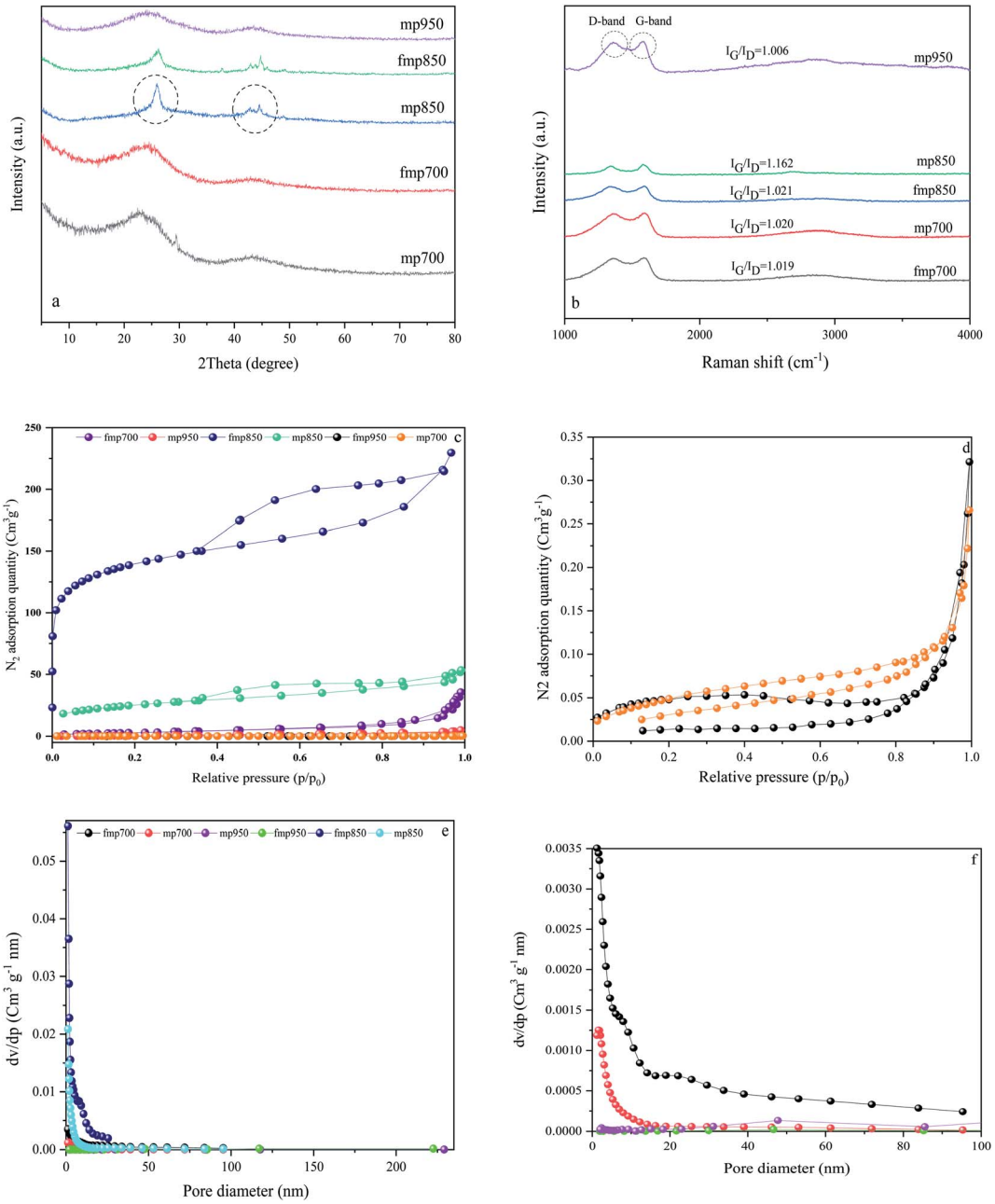

Fig. 3 XRD (a), Raman (b), N_2 adsorption–desorption (c), magnify the figure of c (including mp700, and fmp950) (d), BJH pore size distributions curves (e) and magnify the figure of e (including fmp700, mp700, fmp950, and mp950) (f) of porous carbons.

Table 1 Detailed textural properties of the synthesized carbon foams

Sample ID	Specific surface area (m^2 g^{-1})	Average pore diameter (nm)	Pore volume (cm^3 g^{-1})	Mesoporous volume (cm^3 g^{-1})	Microporous volume (cm^3 g^{-1})	Yield (%)
mp700	2.2	14.2	0.007	0.001	0.006	49
fmp700	10.8	20.2	0.055	0.001	0.055	43
mp850	88.4	3.7	0.081	0.023	0.058	31
fmp850	499.5	2.9	0.355	0.174	0.181	13
mp950	4.2	5.4	0.005	0.005	0.0001	44
fmp950	3.9	6.4	0.006	0.005	0.0002	46

synthesized foams pyrolyzed at 700 and 950 °C in Fig. 3(a) correspond to the graphitic (002) and (100) planes of carbon, respectively.[39] The turbostratic nature of these carbon compounds can be inferred from the broadness and weak intensity of the (002) and (100) peaks in the synthesized samples at 750 and 950 °C.[10,17] In the mp850 and fmp850 samples, the width of the peaks has been decreased, indicating that the graphitization degree has been enhanced. Slightly blue shifts of (002) and (100) diffraction peaks in mp850 and fmp850 are due to the decrease in the interplanar spacing.[40] As the temperature rises to 950 °C, the graphitization level of the structure decreases, which could be due to the collapse of the cavity walls.[41] From the Raman spectra in Fig. 3(b) it can be possible to further declare the graphitization level of the synthesized carbons. This can be determined by comparing the intensity ratios of the disordered diamond (D) band to the ordered graphitic (G) band of the Raman spectra. All samples have D and G bands that are centered at 1355 cm^{-1} and 1585 cm^{-1}, respectively, corresponding to the sp^3 carbons in the disordered carbon structures and sp^2 hybridized carbons in graphitic carbon structures.[42] Furthermore, the presence of a 2D-band at about 2800 cm^{-1} indicates a greater degree of graphitization and is due to the interaction between graphite planes, in the carbon structure.[43] The relative ratio of the G band to the D band (I_G/I_D) is commonly used to determine the degree of graphitization in porous carbons.[44] As the mentioned ratios show, the intensity ratios of G to D bands (I_G/I_D) of all the samples are larger than 1, indicating a proper graphitization on the carbon surface.[17]

Textural properties, including the specific surface area, pore-volume, and average pore diameter of the synthesized carbons extracted from N_2 adsorption–desorption and pore size distribution analyses, Fig. 3(c)–(f) were collected in Table 1. From the N_2 adsorption–desorption results it is clear that the pyrolyzation temperature has a remarkable effect on the textural properties of the synthesized carbons. Increasing the pyrolyzation temperature from 700 °C to 850 °C results in the increase in the specific surface area from 2.2 $m^2\ g^{-1}$ to 88.4 $m^2\ g^{-1}$ in carbon foams synthesized without Pluronic F127 and from 10.8 $m^2\ g^{-1}$ to 499.5 $m^2\ g^{-1}$ for carbon foams synthesized using Pluronic F127 as the soft template. Further increase in the pyrolyzation temperature to 950 °C led to a pronounced decrease in the specific surface area to 4.2 $m^2\ g^{-1}$ and 3.9 $m^2\ g^{-1}$ for synthesized carbons without and with using Pluronic F127, respectively. It seems that according to the results (Table 1), two factors have played the creation of pores and specific surface areas (removal of F127 and activation through carbon dioxide). The effectiveness of carbon dioxide on the activation process can be declared from the mp850 surface characteristics and fmp850 can demonstrate the effectiveness of Pluronic F127. The reaction of carbon dioxide with the surface carbon atoms (Boudouard reaction) can resemble shoveling or etching of the surface. This shoveling or etching process increases the specific surface area of the synthesized carbons. The minimum temperature required for the beginning of the Boudouard reaction in which the Gibbs free energy change of this reaction becomes negative is 705 °C. Therefore, CO_2 gases produced at a temperature below this temperature are not effective for the activation process.[45] Also, during the pyrolyzation treatment, the elimination of Pluronic F127 soft templates (porosity formation) takes place which increases of the specific surface area. From the N_2 adsorption–desorption results it seems that the elimination of the soft templates beginning and continuing at temperatures greater than 700 °C can justify the low specific surface area and pore volume of fmp700. Low specific surface area and pore volume of mp950 and fmp950 can be attributed to the lack of CO_2 gas in the reaction chamber and also the collapse of the porous carbon structure.[46,47] Comparison of mp850 and fmp850 synthesized porous carbon with other synthesized carbons in Table 1, confirms that during the pyrolyzation treatment at 850 °C, both micropores and mesopores volume increased. The simultaneous increase in the micropores and mesopores volume shows that new pore creation and pore widening took place at the same time and that the micropore production did not compromise the mesopores' structure. With simultaneous consideration of Fig. 3(a) and (b), it can be deduced that fmp850 has the highest graphitization level. As summarized in Table 1, the fmp850 has the highest specific surface area (499.51 $m^2\ g^{-1}$), the highest yield (13%), and the highest amount of total pore volume (0.355 $cm^3\ g^{-1}$). The higher specific surface area is consistent with the higher defected carbon structures *i.e.*, higher I_d in the Raman spectra. Therefore, approximately the same I_G to I_d level of all the synthesized carbons indicates that the I_G (the level of graphitization) of fmp850 must be higher than other synthesized carbons. This better graphitization can also be approved by the sharp (002) and (100) graphitic peaks in the X-ray diffraction pattern of fmp850.

The addition of simple functional groups to the porous carbons will increase their affinity for acidic CO_2 molecules.[19] Oxygen contains functional groups that are often polar in nature and increase the degree of hydrophilicity of the carbon surface. The hydrophilicity of the pore surface increases the competition between CO_2 and moisture adsorption, which in turn reduces the adsorption capacity.[19] Also, a nitrogen atom has the same atomic radius as a carbon atom and shares five valence electrons with it. As a result, the physical and chemical properties of the carbon structure, including electronic properties, electrical conductivity, basicity, oxidation, and catalytic efficiency, can be modified by regulating the doping number of the nitrogen atom.[48] The surface chemical properties of the porous carbons have been depicted in Fig. 4. FTIR curves are used to describe the functional groups in the structure. Fig. 4(a) shows the FTIR curves of fmp before pyrolysis, fmp850, and mp850. Fig. 3(a) illustrates a peak at around 3430 (cm^{-1}), which is commonly assigned to stretching vibration of hydroxyl bands.[49] The peak at 3000 cm^{-1} indicates the C–H bond. The 1700 (cm^{-1}) band is correlated to the stretching of C=O bonds in carboxyl groups. Furthermore, peaks between 1438 to 1654 (cm^{-1}) correlate to the vibration of C=C, and C–N bonds, demonstrating that N atoms were successfully incorporated into the structure and it is clear that after pyrolysis due to high temperatures, the peaks related to nitrogen have weakened. As it is known, after pyrolysis, C–H, C=C and C–N bonds are

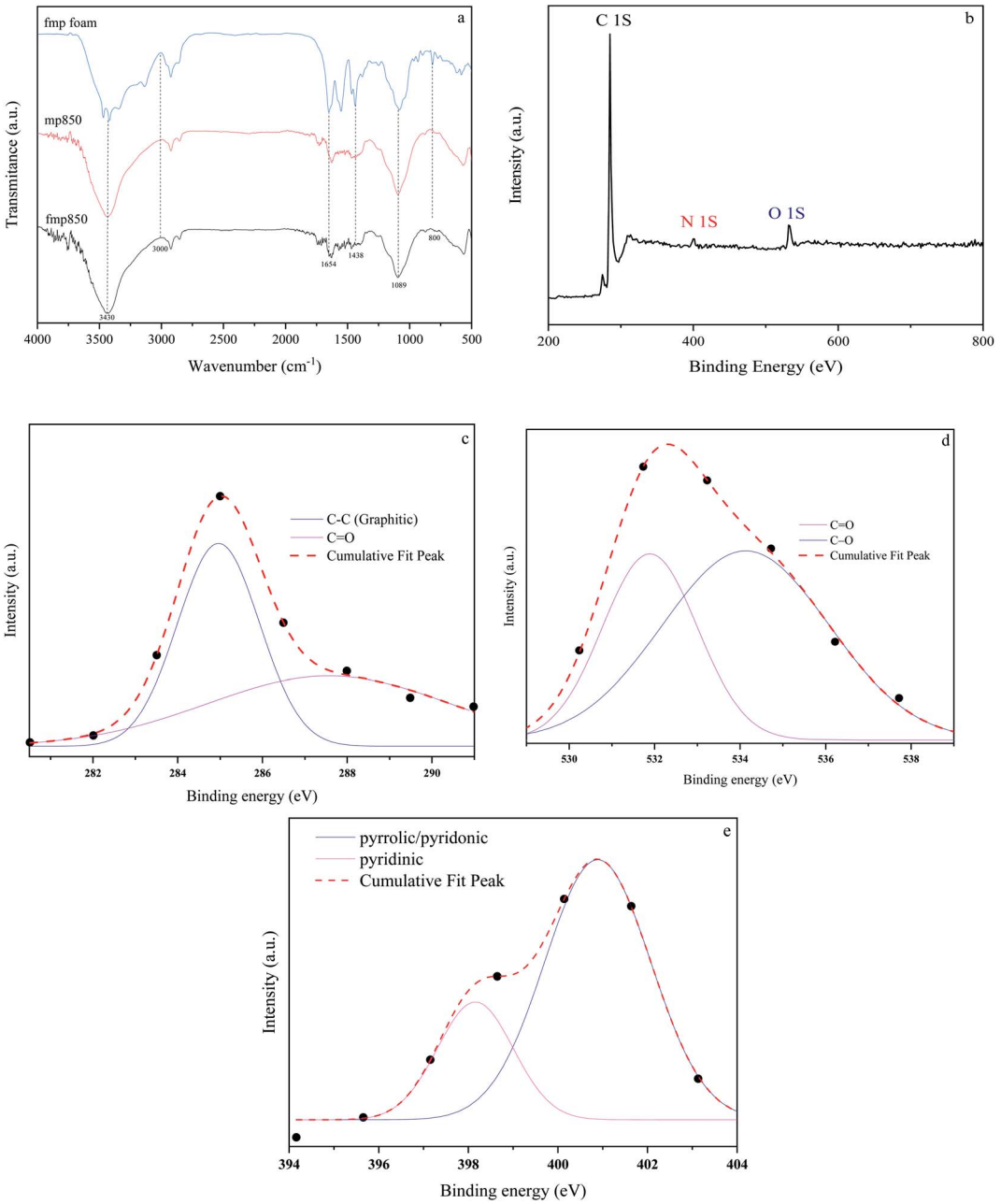

Fig. 4 FTIR transmission of fmp850, mp850, and fmp before pyrolysis (a), XPS survey spectrum of fmp850 sample showing the presence of C, N and O elements (b), C 1s (c), O 1s (d), and N 1s (e) peak deconvolution.

reduced and hydroxyl bonds are formed, which can lead to an increase in the amount of oxygen in the structure. Another set of broad and strong peaks at 1090 (cm^{-1}) might be attributed to the vibration of C–O bond (phenolic). A tiny peak at 880 (cm^{-1}) is caused by C–O–C bonds. Fmp850 is aromatic and has an oxygenated functional group including phenolic and carboxylic acid groups, which give the surface a negative charge. All of these functional groups can boost CO_2 adsorption capacity.[30,50]

The surface composition and atomic percentage of the fmp850 porous carbon material were then investigated using XPS. As shown in Fig. 4(b), three peaks at 285 eV, 400 eV and 532 eV correspond to C 1s (61.2%), N 1s (9.3%) and O 1s (29.5%). According to the high-resolution elemental spectra (Fig. 4(c)), the C 1s spectrum can be deconvoluted into two distinct peaks, each of which is attributable to sp^3 C–C (284.9 eV), C=O (287.5 eV). The O 1s spectra can be fitted into two peaks corresponding to C=O (531.4 eV) and C–O (534.4 eV) (Fig. 4(d)).[34,51–53] Furthermore, as shown in Fig. 4(e), the core level spectra of N 1s may be deconvoluted into two peaks at 398.4, 401 eV. The peaks at 398.4 and 401 eV represent pyridinic and pyrrolic/pyridonic signals, respectively. The pyrrolic and pyridonic cannot be separated from one another using XPS measurements. However, due to the presence of oxygen in the porous carbon structure and the fact that pyridonic is more stable than pyrrolic. According to the results of other researches, pyridonic and pyridinic groups are suitable for

adsorption of CO_2, due to the increase of active sites and stronger interactions that occur between nitrogen groups and CO_2 molecules.[54]

The surface morphology and crystalline analysis of fmp850 have been shown in Fig. 4. The surface morphology of the fmp850 specimen by using a field emission scanning electron microscope (FESEM) is shown in Fig. 5(a) and (b). As can be seen, a graphite cauliflower structure is observed.[55] It can be shown that the size distribution of the pores, which is one of the most important factors deciding its applicability, occurred at random on the sample surface. In Fig. 5(a) and (b), micropores, mesopores, and macropores are identified and show a hierarchical porous structure with larger pores created at high temperatures. The diffusion and mass transfer of molecules are enhanced by the hierarchical porous carbon structure.[56] The formation of pores produced a large surface area as well as access to the material's interior. Rougher textures with heterogeneous with the presence of compact graphitic and microporous carbon aggregates and porous with many cavities can be seen.[57,58]

The TEM images, which reveal the formation of crystallinity of the porous structure, can be used to verify the manufacturing of the fmp850. The presence of porosity with an interconnected and worm-like structure is evident in the TEM images.[41,59]

By comparing these two samples, more order graphite plates can be seen in the fmp850 than in the fmp950 sample, which indicates the collapse of the structure at much higher temperatures. This is in line with the results of XRD and Raman.

3.2. CO_2 adsorption performance

The plot of CO_2 uptake for the fmp850 sample under 0–1 bar pressure and 0 °C is shown in Fig. 6. The adsorption rate at 1 bar pressure and 273 K temperature is 3.1 mmol g^{-1}, which is

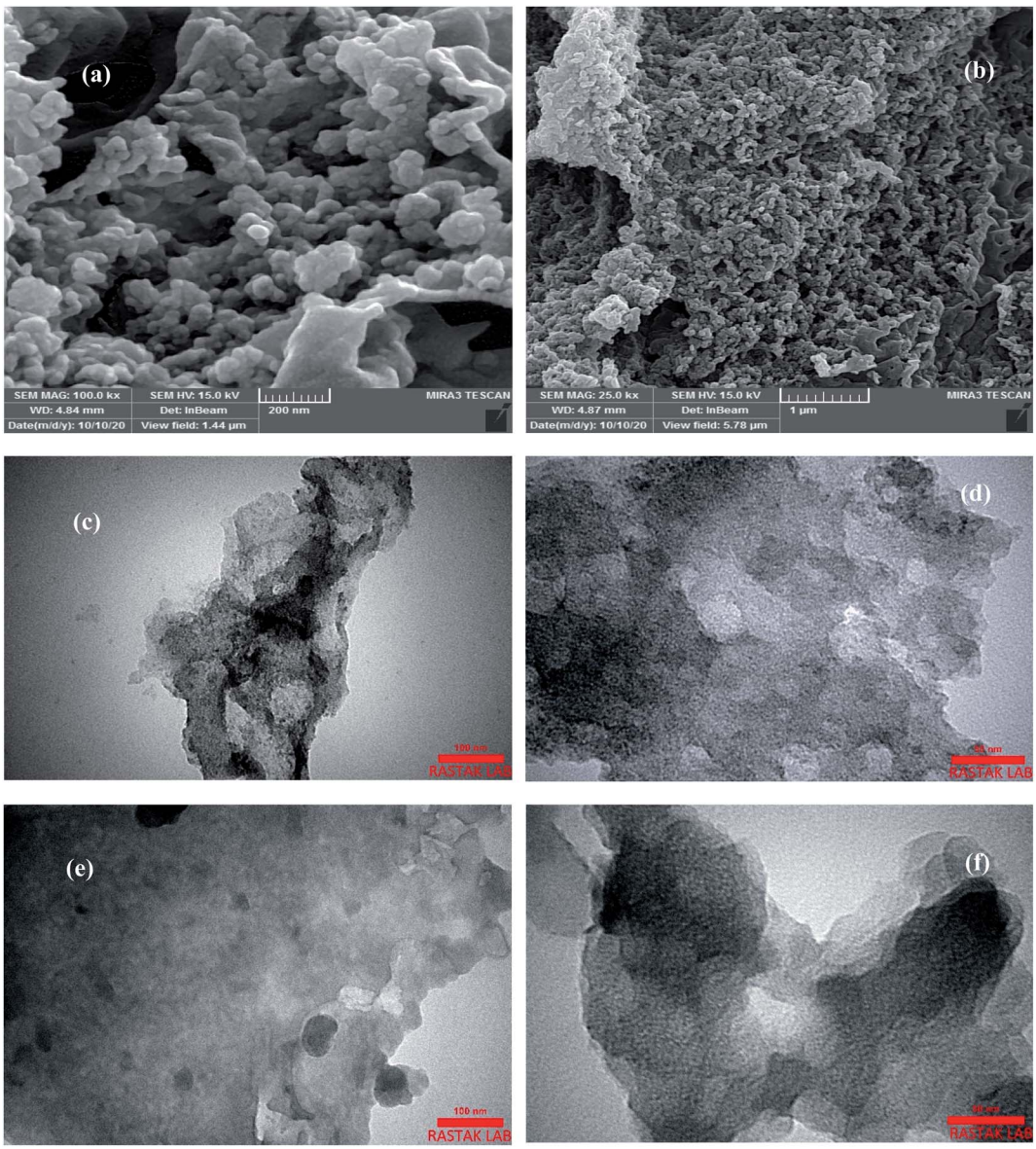

Fig. 5 FESEM images of cauliflower-like texture of fmp850 (a), (b) and TEM images of worm-like structure fmp850 (c), (d) and fmp950 (e), (f).

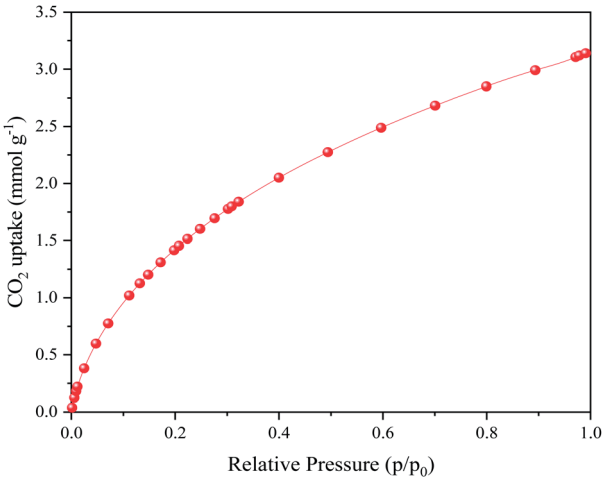

Fig. 6 CO_2 adsorption at 273 K under pressure 0–1 bar on the fmp850.

comparable to other porous carbons. The fmp850 sample was selected as the sample for adsorption due to its higher specific surface area and suitable pore size distribution. CO_2 adsorption rises with increasing pressure without revealing adsorption saturation, showing that the adsorbent can support greater CO_2 adsorption at higher pressures. The formation of nitrogen-containing groups like pyridonic, on carbon surfaces and micropores, which may improve the affinity of carbon materials for CO_2 uptake.[60,61] The initial consequence of nitrogen doping is that it promotes a larger density of N-doped basic active sites for enhanced van der Waals interactions between nitrogen functional groups and CO_2 molecules, which increases adsorption capacity.[62] CO_2 adsorption could be enhanced by the existence of a microporous structure and strong interactions between CO_2 molecules and the framework (particularly N-containing groups) *via* H-bonding or dipole–quadrupole interactions in N-enriched porous carbons.[63] The strong hydrogen-bonding interactions between CO_2 molecules and hydrogen atoms (from CH and NH groups) on the carbon surface are greatly enhanced by the intercalation of N atoms into the carbon framework, which acts for the excellent CO_2 capture behavior of N-doped porous carbons. Also, the strong dipolar C=O bonds give the CO_2 molecules a significant electric quadrupole moment. The N doping introduces polar groups into the carbon skeleton, which can cause local polarization/charge separation. As a result, N-containing compounds improve performance in the presence of strong quadrupole interactions between CO_2 molecules and the surface.[53,64] As previously stated, narrow microporosity greatly affects CO_2 adsorption at 298 K and pressures up to 1 bar, and in many cases, a linear connection between equilibrium adsorption capacity and narrow micropore volume may be established. In this regard, it is worth noting that, while micropores are the most essential adsorption factors for CO_2, associated meso and macropores are also significant for adsorption purposes since they usually contribute to the diffusion of the gas from the bulk carbon matrix.[65–67]

3.3. Kinetic and thermodynamic analysis

Micropores, mesopores, and adsorbent surface are play key role for review of various energy in gas adsorption by permeable materials. The adsorption mechanism is related to physical and chemical structure affect of the adsorbent, as per investigation of the uptake kinetic. We investigated diverse theoretical kinetic models, including pseudo-first-request, pseudo-second-request, Elovich, and fragmentary request as below equations (eqn (1)–(4)).[68]

Pseudo-first-order

$$q_t = q_e(1 - e^{-k_1 t}) \quad (1)$$

Pseudo-second-order

$$q_t = (q_e^2 k_s t)/[1 + q_e k_s t] \quad (2)$$

Elovich

$$q_t = (1/\beta \ln(\alpha\beta)) + (1/\beta \ln t) \quad (3)$$

Ritchie second order

$$q_t = q_e - q_e(1 + k_2 t)^{-1} \quad (4)$$

Table 2 Calculated parameters of CO_2 adsorption kinetic models at 6 bar for fmp850

Kinetic models	Parameters	298 K	308 K	318 K
Pseudo-first-order	q_e (mg g^{-1})	323.611	162.429	172.823
	k_f (1 min^{-1})	0.013	0.004	0.004
	R^2	0.8182	0.8937	0.9412
Pseudo-second-order	q_e (mg g^{-1})	334.918	175.337	185.798
	k_s (1 min^{-1})	0.000069	0.000036	0.000037
	R^2	0.9422	0.9505	0.9789
Elovich	α (mg g^{-1} min^{-1})	1.70859	0.01664	0.01793
	β (g mg^{-1})	28.65	24.14	25.28
	R^2	0.9771	0.9929	0.9844
Ritchie second order	q_e (mg g^{-1})	334.918	175.338	185.798
	k_2 (1 min^{-1})	0.023	0.006	0.007
	R^2	0.9422	0.9505	0.97888

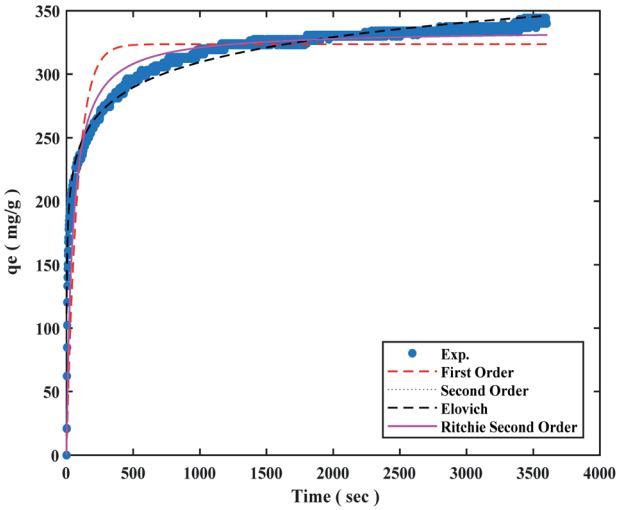

Fig. 7 CO_2 adsorption experiment of fmp850 *via* fitting desirable kinetic models at 298 K.

The pseudo-first-order and the second-order kinetic models are illustrated the chemisorption process as the adsorption controlling factor *via* the reversible adsorption interaction the adsorbent surface.[69] Due to predicting kinetic parameters is complex, we applied the typical method with the adjust experimental data to mentioned models for choose the best one.[70]

The Elovich kinetic model was found to be the best match based on correlation coefficient values (R^2) in the range of 0.9771 to 0.9929 at 6 bar (298, 308, and 318 K), and related kinetic parameters are presented in Table 2. The CO_2 adsorption kinetic model at 298 K under 6 bar pressure was also fitted to the experiment data and presented in Fig. 7.

The laws of thermodynamics are used to calculate the entropy (ΔS^0) and the Gibbs free energy (ΔG^0) parameters using absolute temperature T (°K) and, the following equations. The adsorption enthalpy was evaluated using the Van't Hoff equation, eqn (7), and from the unification of two equations, eqn (5) and (6):[71]

$$\Delta G^0 = \Delta H^0 - T\Delta S^0 \quad (5)$$

$$\Delta G^0 = -RT \ln K_d \quad (6)$$

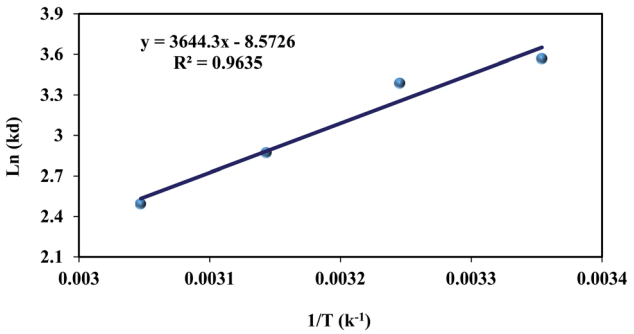

Fig. 8 CO_2 experimental Van't Hoff plot on fmp850.

Table 3 Thermodynamic parameters of the fmp850 in CO_2 adsorption at 6 bar

ΔH (kJ mol^{-1})	ΔS (kJ mol^{-1} K^{-1})	ΔG (kJ mol^{-1})			
		298 K	308 K	318 K	328 K
−30.03	−0.071	−9.049	−8.337	−7.624	−6.911

$$\ln K_d = \frac{\Delta S^0}{R} - \frac{\Delta H^0}{RT} \quad (7)$$

where R is gas constant (8.314 (J mol^{-1} K^{-1})), enthalpy (ΔH^0) is slope and entropy is intercept that they are obtained from the plotting of ln K_d against $1/T$. Thermodynamic parameters were investigated in temperature ranges from 273 to 328 K at 6 bar. The Van't Hoff plot of fmp850 is disply in Fig. 8 and the positive slope of the ln K_d curve shows the adsorption process is exothermic.

Table 3 shows the results of the estimated CO_2 thermodynamic parameters. The physisorption process was represented using a value of less than 20 (kJ mol^{-1}) since the chemisorption process was illustrated using a value of more than 40 (kJ mol^{-1}).[68] The ΔS^0 is a display of the randomized and organized gas–solid interfaces, and in this case of $\Delta S^0 < 0$ representing less randomness.[70] The negative values of Gibbs free energy (ΔG^0) and (ΔS^0), indicating that the adsorption process is exothermic and spontaneous. The present thermodynamic results show that low enthalpy values indicate physical absorption, and it is in step with different preceding studies on this field.[68–71]

3.4. Equilibrium adsorption isotherms

In Fig. 9, the CO_2 adsorption isotherms were plotted using the Langmuir, Freundlich, Dubinin Radushkevich (D–R), and Temkin equations at 308 K and pressures ranging from 3.25 to

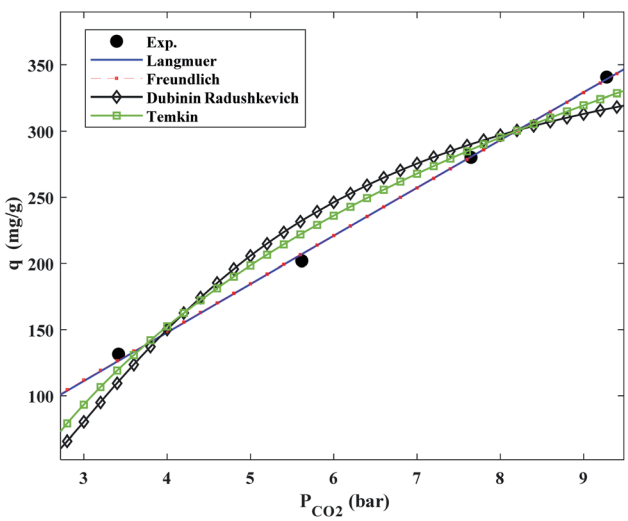

Fig. 9 Comparison isotherms models *vs.* fmp850 experimental data for CO_2 adsorption at 308 K.

Table 4 Theoretical isotherm models of CO_2 adsorption at 6 bar for fmp850[a]

Models	Parameters	298 K	308 K	318 K
Langmuir $q_e = q_m k_L P(1 + k_L P)$	q_m	625.2	16 150.1	2512.4
	k_L	0.152	0.001	0.012
	R^2	0.9991	0.9992	0.9953
Freundlich $q_e = k_F P_e^{1/n}$	k_f	139.1	36.751	37.237
	n	1.934	1.002	1.008
	R^2	0.9967	0.9988	0.9939
Dubinin Radushkevich $q_e = q_m e^{-\lambda\omega 2}$	q_m	440.827	379.281	321.122
	λ	1.138	2.012	2.057
	ω	0.657	0.502	0.399
	R^2	0.9927	0.9642	0.9321
Temkin $q_e = B \times \log(A) + B \times \log(c)$	A	1.047	0.421	0.497
	B	152.017	199.028	162.284
	R^2	0.9995	0.9844	0.9812

[a] Where q_e is the value of CO_2 adsorption capacity (mmol g^{-1}), q_m is the max adsorption value of CO_2 (mmol g^{-1}), P is the equilibrium pressure (bar), k_F is the Freundlich model constants ((mmol g^{-1}) $(bar^{-1})^{1/n}$) and, n is Freundlich isotherm constant. λ is (D–R) model constant (mol^2 J^{-2}), ω is Polanyi potential (J mol^{-1}), A is the Temkin model constant (L mol^{-1}), and B is the first virial coefficient ($B = RTb_T^{-1}$); b_T^{-1} (J mol^{-1}).

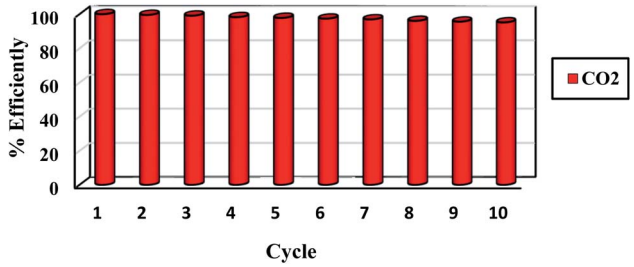

Fig. 10 Recycling performance of the fmp850 sample for CO_2 adsorption.

9.25 bar. The findings showed that increasing the uptake pressure increased the rate of CO_2 adsorption. Table 4 shows the experimental results and related to R^2 correlation coefficients for all coefficients of isotherm parameter models.

As the temperature was raised, the adsorption values dropped, suggesting an exothermic CO_2 adsorption tendency. While all of the isotherm models agreed with the experimental results, when fitted to the data, the Langmuir isotherm model exhibited the greatest correlation coefficient (R^2) values. Furthermore, the energy parameters of two isotherm models established by D–R and b_T Temkin provide valuable data, where ω is the mean adsorption free energy and is the heat of adsorption.

The normal physisorption of CO_2 adsorption is shown by average λ values in the 1–2 (kJ mol^{-1}) range.[71] Based on the findings in Table 4, the Freundlich constant, n, in the range of 1 to 1.93, demonstrates the attractiveness of physisorption. The adsorption process is multi-layer, with CO_2 absorbed and permeated in the surface and interior layers of the fmp850, according to the findings. Langmuir > Freundlich > D–R > Temkin was the order of efficacy of the mentioned theoretical

Table 5 Comparison of adsorption capacity of different precursors with specific surface area and different pyrolysis temperature at 273 K and 1 bar

Precursor (–)	Pyrolysis temperature (°K)	Specific surface area (m^2 g^{-1})	Adsorption capacity (mmol g^{-1})	Adsorption capacity/specific surface area (μmol m^{-2})	Ref.
Poplar catkin	1073	1024.8	2.8	2.73	73
Pineapple waste	973	1076.3	5.32	4.94	74
Lotus leaf	823	1883	3.58	1.90	75
Casein	1073	1080	3.5	3.24	76
Walnut shell	773	1721	3.17	1.84	77
Celtuce leaves	873	3404	6	1.76	78
Peanut shell	1000	1893	7.12	3.76	79
Hazelnut shell	823	1600	6.43	4.01	80
Water caltrop shell	873	2194	5.97	2.72	81
Graphene	973	1296	2.52	1.94	82
Lotus stalk	873	1188	5.11	4.30	83
Commercial phenolic	873	2200	7.47	3.39	84
Black locust	923	1175	2.79	2.37	85
Pollen	873	1460	5.63	3.85	86
Pectin	1123	499.51	3.1	6.20	This work

isotherms in the explanation and prediction of adsorption behavior, according to the nonlinear (R^2) values determined in Table 4 and by the nonlinear regression technique.[70,72]

4. Regeneration performance of fmp850

One of the most important aspects is the reuse of sorbent for economic reasons. The regeneration process for 0.5 g sorbent was evaluated at a pressure of less than 2 bar. Ten adsorption/desorption cycles at 298 K at 6 bar were recorded for the CO_2 adsorption process, which was then regenerated at 460 K in a vacuum oven for 5 hours. The adsorbent potential does not vary much after each loop, as seen in Fig. 7. The sorbent's adsorption performance was lowered from 100% to 98% after 10 cycles. As result, the sorbent can be employed in industrial applications as a low-cost and cost-effective adsorbent based on the effects of the regeneration process (Fig. 10).

5. Comparison of various porous carbons

The adsorption capacity of the fmp850 sample is compared with other biomass-based porous carbon samples at 273 K and 1 bar pressure in Table 5. The ratio of the adsorption side to the amount of specific surface area for each sample is given in Table 5. As it turns out, the highest adsorption ratio to the specific level is related to the current study. These samples were all activated by an foreign agent, but the sample studied in this study did not have any activation by an external agent.

6. Conclusion

In summary, the synthesis of porous carbon using pectin and a source of melamine was utilized to add nitrogen to the structure. Furthermore, F127 as mold was used to create porosity. fmp850 was used for CO_2 adsorption at 273 K and 1 bar pressure that showed an adsorption capacity of 3.1 (mmol g^{-1}). This result indicated that fmp850 with a relatively low specific surface area had a higher adsorption ratio to specific surface area (6.20 μmol m^{-2}) than other porous carbons. One of the reasons for proper adsorption is the high presence of nitrogen in the structure, particularly pyridonic nitrogen, as well as the suitable percentage of micropores in the sample. Moreover, these characterizations indicated that the role of parameters such as heteroatom added to the structure for CO_2 uptake. Besides, the volume of micropores played a greater role than the high specific surface area for CO_2 adsorption. The kinetic and thermodynamic analysis results show that low enthalpy values indicate physisorption for the adsorption process and the Elovich model was found the best kinetic model. In general, with the results of this research, due to the lower cost, the use of a cheap source of nitrogen such as melamine, proper adsorption relative to the specific surface area, and the lack of reagent, this adsorbent is promising for CO_2 uptake. Eventually, we trust that our method can promote the usage of pectin-melamine nitrogen-enriched for synthesizing high-overall performance porous carbons in industrial cases.

Abbreviations

K_L Langmuir model constant (bar^{-1})
k_f Rate constant of adsorption for the Pseudo-first-order (1 min^{-1})
k_s Rate constant of adsorption for the first-order model (g $mmol^{-1}$ min^{-1})
K_d Distribution coefficient
m Mass of gas adsorbed (mg)
P Pressure (bar)
P_0 Saturated vapor pressure (bar)
q Adsorption capacity (mmol g^{-1})
q_e Equilibrium adsorption capacity (mmol g^{-1})
q_m Maximum adsorption (mmol g^{-1})
q_t Adsorption capacity at specified time t (mmol g^{-1})
R Universal gas constant (8.314 J mol^{-1} K^{-1})
R^2 Correlation coefficient (%)
T Temperature (K), (C)
t Time (s)

Greek symbols

α Parameter value of Elovich model (mmol g^{-1} min^{-1})
β Parameter value of Elovich model (g $mmol^{-1}$)

Acronyms

CO_2	Carbon dioxide
CCS	Carbon capture and storage
FTIR	Fourier transform infra-red
FESEM	Field emission scanning electron microscopy
TEM	Transmission electron microscopy
PSD	Pore size distribution
TG	Thermo gravimetric
XPS	X-ray photoelectron spectroscopy
XRD	X-Ray diffraction

Conflicts of interest

The authors state that they have no known competing financial interests or personal ties that could appear to have influenced the work described in this study.

References

1 B. Kaur, R. K. Gupta and H. Bhunia, Chemically activated nanoporous carbon adsorbents from waste plastic for CO2 capture: Breakthrough adsorption study, *Microporous Mesoporous Mater.*, 2019, **282**, 146–158.

2 J. Singh, S. Basu and H. Bhunia, CO2 capture by modified porous carbon adsorbents: Effect of various activating agents, *J. Taiwan Inst. Chem. Eng.*, 2019, **102**, 438–447.
3 A. González, M. Plaza, F. Rubiera and C. Pevida, Sustainable biomass-based carbon adsorbents for post-combustion CO2 capture, *Chem. Eng. J.*, 2013, **230**, 456–465.
4 J. Singh, H. Bhunia and S. Basu, Synthesis of porous carbon monolith adsorbents for carbon dioxide capture: Breakthrough adsorption study, *J. Taiwan Inst. Chem. Eng.*, 2018, **89**, 140–150.
5 S. Valiani, N. Tahouni and M. H. Panjeshahi, Optimization of pre-combustion capture for thermal power plants using Pinch analysis, *Energy*, 2017, **119**, 950–960.
6 Y.-C. Chiang and R.-S. Juang, Surface modifications of carbonaceous materials for carbon dioxide adsorption: a review, *J. Taiwan Inst. Chem. Eng.*, 2017, **71**, 214–234.
7 M. Pardakhti, T. Jafari, Z. Tobin, B. Dutta, E. Moharreri, N. S. Shemshaki, S. Suib and R. Srivastava, Trends in solid adsorbent materials development for CO2 capture, *ACS Appl. Mater. Interfaces*, 2019, **11**(38), 34533–34559.
8 X. Liu, F. Gao, J. Xu, L. Zhou, H. Liu and J. Hu, Zeolite@mesoporous silica-supported-amine hybrids for the capture of CO2 in the presence of water, *Microporous Mesoporous Mater.*, 2016, **222**, 113–119.
9 A. Kumar, A. Rana, G. Sharma, S. Sharma, M. Naushad, G. T. Mola, P. Dhiman and F. J. Stadler, Aerogels and metal–organic frameworks for environmental remediation and energy production, *Environ. Chem. Lett.*, 2018, **16**(3), 797–820.
10 M. Asgarpour Khansary, M. A. Aroon and S. Shirazian, Physical adsorption of CO2 in biomass at atmospheric pressure and ambient temperature, *Environ. Chem. Lett.*, 2020, **18**(4), 1423–1431.
11 M. Subramaniam, S. Satish, J. M. Solomon and R. Sathyamurthy, Numerical and experimental investigation on capture of CO2 and other pollutants from an SI engine using the physical adsorption technique, *Heat Tran.*, 2020, **49**(5), 2943–2960.
12 H. Sharma and A. Dhir, Capture of carbon dioxide using solid carbonaceous and non-carbonaceous adsorbents: a review, *Environ. Chem. Lett.*, 2020, 1–23.
13 Q. Liu, P. He, X. Qian, Z. Fei, Z. Zhang, X. Chen, J. Tang, M. Cui, X. Qiao and Y. Shi, Enhanced CO2 adsorption performance on hierarchical porous ZSM-5 zeolite, *Energy Fuels*, 2017, **31**(12), 13933–13941.
14 S. Nandi, R. Maity, D. Chakraborty, H. Ballav and R. Vaidhyanathan, Preferential Adsorption of CO2 in an Ultramicroporous MOF with Cavities Lined by Basic Groups and Open-Metal Sites, *Inorg. Chem.*, 2018, **57**(9), 5267–5272.
15 R. Adams, C. Carson, J. Ward, R. Tannenbaum and W. Koros, Metal organic framework mixed matrix membranes for gas separations, *Microporous Mesoporous Mater.*, 2010, **131**(1–3), 13–20.
16 B. Arstad, H. Fjellvåg, K. O. Kongshaug, O. Swang and R. Blom, Amine functionalised metal organic frameworks (MOFs) as adsorbents for carbon dioxide, *Adsorption*, 2008, **14**(6), 755–762.
17 X. Ma, C. Su, B. Liu, Q. Wu, K. Zhou, Z. Zeng and L. Li, Heteroatom-doped porous carbons exhibit superior CO2 capture and CO2/N2 selectivity: understanding the contribution of functional groups and pore structure, *Sep. Purif. Technol.*, 2021, **259**, 118065.
18 Z. Li, K. Guo and X. Chen, Controllable synthesis of nitrogen-doped mesoporous carbons for supercapacitor applications, *RSC Adv.*, 2017, **7**(49), 30521–30532.
19 D. Saha and M. J. Kienbaum, Role of oxygen, nitrogen and sulfur functionalities on the surface of nanoporous carbons in CO2 adsorption: a critical review, *Microporous Mesoporous Mater.*, 2019, **287**, 29–55.
20 C. Song, M. Liu, W. Ye, Y. Liu, H. Zhang, R. Lu and S. Zhang, Nitrogen-Containing Porous Carbon for Highly Selective and Efficient CO2 Capture, *Energy Fuels*, 2019, **33**(12), 12601–12609.
21 X. F. Wang, L. Xiong, L. Li and J. J. Zhong, Effect of heat treatment temperature on CO2 capture of nitrogen-enriched porous carbon fibers, *Greenh. Gases*, 2020, **10**(2), 461–471.
22 M. V. Hossein Mashhadimoslem, M. Safarzadeh, A. Ghaemi, F. Fathalian and M. Ali, Development of Predictive Models for Activated Carbon Synthesis from Different Biomass for CO2 Adsorption Using Artificial Neural Networks, *Ind. Eng. Chem. Res.*, 2021, **60**(38), 13950–13966.
23 D. Wu, J. Liu, Y. Yang and Y. Zheng, Nitrogen/Oxygen Co-Doped Porous Carbon Derived from Biomass for Low-Pressure CO2 Capture, *Ind. Eng. Chem. Res.*, 2020, **59**(31), 14055–14063.
24 X. Zhang, S. Zhang, H. Yang, Y. Feng, Y. Chen, X. Wang and H. Chen, Nitrogen enriched biochar modified by high temperature CO2–ammonia treatment: characterization and adsorption of CO2, *Chem. Eng. J.*, 2014, **257**, 20–27.
25 S. Deng, H. Wei, T. Chen, B. Wang, J. Huang and G. Yu, Superior CO2 adsorption on pine nut shell-derived activated carbons and the effective micropores at different temperatures, *Chem. Eng. J.*, 2014, **253**, 46–54.
26 W. Xiong, J. H. Kang and Y. Jung, Preparation of nitrogen-doped porous carbon from melamine-formaldehyde resins crosslinked by phytic acid, *Int. J. Electrochem. Sci.*, 2018, **13**, 852–862.
27 D. Salinas-Torres, A. F. Léonard, V. Stergiopoulos, Y. Busby, J.-J. Pireaux and N. Job, Effect of nitrogen doping on the pore texture of carbon xerogels based on resorcinol-melamine-formaldehyde precursors, *Microporous Mesoporous Mater.*, 2018, **256**, 190–198.
28 M. Chen, T. Le, Y. Zhou, F. Kang and Y. Yang, Thiourea-induced N/S dual-doped hierarchical porous carbon nanofibers for high-performance lithium-ion capacitors, *ACS Appl. Energy Mater.ACS Appl. Energy Mater.*, 2020, **3**(2), 1653–1664.
29 B. Zhu, C. Shang and Z. Guo, Naturally nitrogen and calcium-doped nanoporous carbon from pine cone with superior CO2 capture capacities, *ACS Sustainable Chem. Eng.*, 2016, **4**(3), 1050–1057.

30 L. Shao, Y. Sang, N. Liu, J. Liu, P. Zhan, J. Huang and J. Chen, Selectable Microporous Carbons Derived from Poplar Wood by Three Preparation Routes for CO2 Capture, *ACS Omega*, 2020, **5**(28), 17450–17462.

31 W. Zhang, L. Y. Zhang, X. J. Zhao and Z. Zhou, Citrus pectin derived porous carbons as a superior adsorbent toward removal of methylene blue, *J. Solid State Chem.*, 2016, **243**, 101–105.

32 R. J. White, V. L. Budarin and J. H. Clark, Pectin-derived porous materials, *Chem.–Eur J.*, 2010, **16**(4), 1326–1335.

33 Y. Zhou, X. Ren, Y. Du, Y. Jiang, J. Wan and F. Ma, In-situ template cooperated with urea to construct pectin-derived hierarchical porous carbon with optimized pore structure for supercapacitor, *Electrochim. Acta*, 2020, **355**, 136801.

34 Y. Ma, S. You, B. Jing, Z. Xing, H. Chen, Y. Dai, C. Zhang, N. Ren and J. Zou, Biomass pectin-derived N, S-enriched carbon with hierarchical porous structure as a metal-free catalyst for enhancing bio-electricity generation, *Int. J. Hydrogen Energy*, 2019, **44**(31), 16624–16638.

35 G. Asimakopoulos, M. Baikousi, C. Salmas, A. B. Bourlinos, R. Zboril and M. A. Karakassides, Advanced Cr (VI) sorption properties of activated carbon produced via pyrolysis of the "Posidonia oceanica" seagrass, *J. Hazard. Mater.*, 2021, **405**, 124274.

36 Y. Meng, D. Gu, F. Zhang, Y. Shi, L. Cheng, D. Feng, Z. Wu, Z. Chen, Y. Wan and A. Stein, A family of highly ordered mesoporous polymer resin and carbon structures from organic−organic self-assembly, *Chem. Mater.*, 2006, **18**(18), 4447–4464.

37 N. Rangelova, L. Aleksandrov and S. Nenkova, Synthesis and characterization of pectin/SiO 2 hybrid materials, *J. Sol-Gel Sci. Technol.*, 2018, **85**(2), 330–339.

38 A. Rehman and S.-J. Park, Tunable nitrogen-doped microporous carbons: delineating the role of optimum pore size for enhanced CO2 adsorption, *Chem. Eng. J.*, 2019, **362**, 731–742.

39 M. Wahid, G. Parte, R. Fernandes, D. Kothari and S. Ogale, Natural-gel derived, N-doped, ordered and interconnected 1D nanocarbon threads as efficient supercapacitor electrode materials, *RSC Adv.*, 2015, **5**(63), 51382–51391.

40 X.-w. YIN and L. Quan, Effects of heat treatment temperature on microstructure and electromagnetic properties of ordered mesoporous carbon, *Trans. Nonferrous Metals Soc. China*, 2013, **23**(6), 1652–1660.

41 A. Wang, K. Sun, R. Xu, Y. Sun and J. Jiang, Cleanly synthesizing rotten potato-based activated carbon for supercapacitor by self-catalytic activation, *J. Clean. Prod.*, 2021, **283**, 125385.

42 M. Wang, X. Xu, Y. Liu, Y. Li, T. Lu and L. Pan, From metal-organic frameworks to porous carbons: a promising strategy to prepare high-performance electrode materials for capacitive deionization, *Carbon*, 2016, **108**, 433–439.

43 H. B. M. Emrooz, M. Maleki and A. Rahmani, Azolla-derived hierarchical nanoporous carbons: from environmental concerns to industrial opportunities, *J. Taiwan Inst. Chem. Eng.*, 2018, **91**, 281–290.

44 W. Chaikittisilp, M. Hu, H. Wang, H.-S. Huang, T. Fujita, K. C.-W. Wu, L.-C. Chen, Y. Yamauchi and K. Ariga, Nanoporous carbons through direct carbonization of a zeolitic imidazolate framework for supercapacitor electrodes, *Chem. Commun.*, 2012, **48**(58), 7259–7261.

45 J. Hunt, A. Ferrari, A. Lita, M. Crosswhite, B. Ashley and A. E. Stiegman, Microwave-Specific Enhancement of the Carbon–Carbon Dioxide (Boudouard) Reaction, *J. Phys. Chem. C*, 2013, **117**(51), 26871–26880.

46 B. Dyatkin and Y. Gogotsi, Effects of structural disorder and surface chemistry on electric conductivity and capacitance of porous carbon electrodes, *Faraday Discuss*, 2014, **172**, 139–162.

47 S. Wang and G. M. Lu, Effects of acidic treatments on the pore and surface properties of Ni catalyst supported on activated carbon, *Carbon*, 1998, **36**(3), 283–292.

48 W. Zhang, Y. Bao and A. Bao, Preparation of nitrogen-doped hierarchical porous carbon materials by a template-free method and application to CO2 capture, *J. Clean. Prod.*, 2020, **8**(3), 103732.

49 Y. V. Fedoseeva, E. V. Lobiak, E. V. Shlyakhova, K. A. Kovalenko, V. R. Kuznetsova, A. A. Vorfolomeeva, M. A. Grebenkina, A. D. Nishchakova, A. A. Makarova and L. G. Bulusheva, Hydrothermal Activation of Porous Nitrogen-Doped Carbon Materials for Electrochemical Capacitors and Sodium-Ion Batteries, *Nanomaterials*, 2020, **10**(11), 2163.

50 X. Xu, T. Yuan, Y. Zhou, Y. Li, J. Lu, X. Tian, D. Wang and J. Wang, Facile synthesis of boron and nitrogen-doped graphene as efficient electrocatalyst for the oxygen reduction reaction in alkaline media, *Int. J. Hydrogen Energy*, 2014, **39**(28), 16043–16052.

51 L. Shi, L. Jin, Z. Meng, Y. Sun, C. Li and Y. Shen, A novel porous carbon material derived from the byproducts of bean curd stick manufacture for high-performance supercapacitor use, *RSC Adv.*, 2018, **8**(70), 39937–39947.

52 S. Gao, L. Ge, T. E. Rufford and Z. Zhu, The preparation of activated carbon discs from tar pitch and coal powder for adsorption of CO2, CH4 and N2, *Microporous Mesoporous Mater.*, 2017, **238**, 19–26.

53 H. Mashhadimoslem, M. Safarzadeh, A. Ghaemi, H. B. M. Emrooz and M. Barzegar, Biomass derived hierarchical porous carbon for high-performance O 2/N 2 adsorption; a new green self-activation approach, *RSC Adv.*, 2021, **11**(57), 36125–36142.

54 A. n. Sánchez-Sánchez, F. Suarez-Garcia, A. Martínez-Alonso and J. M. Tascón, Influence of porous texture and surface chemistry on the CO2 adsorption capacity of porous carbons: acidic and basic site interactions, *ACS Appl. Mater. Interfaces*, 2014, **6**(23), 21237–21247.

55 A. Tabet-Aoul and M. Mohamedi, 3D hierarchical cauliflower-like carbon nanotubes/platinum–tin nanostructure and its electrocatalytic activity for ethanol oxidation, *J. Mater. Chem.*, 2012, **22**(6), 2491–2497.

56 B. Sun, Y. Yuan, H. Li, X. Li, C. Zhang, F. Guo, X. Liu, K. Wang and X. Zhao, Waste-cellulose-derived porous

carbon adsorbents for methyl orange removal, *Chem. Eng. J.*, 2019, **371**, 55–63.

57 X.-L. Zhu, P.-Y. Wang, C. Peng, J. Yang and X.-B. Yan, Activated carbon produced from paulownia sawdust for high-performance CO2 sorbents, *Chin. Chem. Lett.*, 2014, **25**(6), 929–932.

58 J. Tey, M. Careem, M. Yarmo and A. Arof, Durian shell-based activated carbon electrode for EDLCs, *Ionics*, 2016, **22**(7), 1209–1216.

59 D. Li, J. Zhou, Z. Zhang, L. Li, Y. Tian, Y. Lu, Y. Qiao, J. Li and L. Wen, Improving low-pressure CO2 capture performance of N-doped active carbons by adjusting flow rate of protective gas during alkali activation, *Carbon*, 2017, **114**, 496–503.

60 Q. Wu, G. Zhang, M. Gao, L. Huang, L. Li, S. Liu, C. Xie, Y. Zhang and S. Yu, N-doped porous carbon from different nitrogen sources for high-performance supercapacitors and CO2 adsorption, *J. Alloys Compd.*, 2019, **786**, 826–838.

61 T. Liang, C. Chen, X. Li and J. Zhang, Popcorn-derived porous carbon for energy storage and CO2 capture, *Langmuir*, 2016, **32**(32), 8042–8049.

62 S. Balou, S. E. Babak and A. Priye, Synergistic Effect of Nitrogen Doping and Ultra-Microporosity on the Performance of Biomass and Microalgae-Derived Activated Carbons for CO2 Capture, *ACS Appl. Mater. Interfaces*, 2020, **12**(38), 42711–42722.

63 X. Zhang, D. Lin and W. Chen, Nitrogen-doped porous carbon prepared from a liquid carbon precursor for CO 2 adsorption, *RSC Adv.*, 2015, **5**(56), 45136–45143.

64 Z. Zhang, Z. P. Cano, D. Luo, H. Dou, A. Yu and Z. Chen, Rational design of tailored porous carbon-based materials for CO 2 capture, *J. Mater. Chem. A*, 2019, **7**(37), 20985–21003.

65 D. Saha, S. E. Van Bramer, G. Orkoulas, H.-C. Ho, J. Chen and D. K. Henley, CO2 capture in lignin-derived and nitrogen-doped hierarchical porous carbons, *Carbon*, 2017, **121**, 257–266.

66 A. Silvestre-Albero, J. Silvestre-Albero, M. Martínez-Escandell and F. Rodríguez-Reinoso, Micro/mesoporous activated carbons derived from polyaniline: promising candidates for CO2 adsorption, *Ind. Eng. Chem. Res.*, 2014, **53**(40), 15398–15405.

67 J. Patiño, M. C. Gutiérrez, D. Carriazo, C. Ania, J. Fierro, M. L. Ferrer and F. Del Monte, DES assisted synthesis of hierarchical nitrogen-doped carbon molecular sieves for selective CO2 versus N2 adsorption, *J. Mater. Chem. A*, 2014, **2**(23), 8719–8729.

68 F. Raganati, M. Alfe, V. Gargiulo, R. Chirone and P. Ammendola, Isotherms and thermodynamics of CO2 adsorption on a novel carbon-magnetite composite sorbent, *Chem. Eng. Res. Des.*, 2018, **134**, 540–552.

69 V. K. Singh and E. A. Kumar, Comparative studies on CO2 adsorption kinetics by solid adsorbents, *Energy Proc.*, 2016, **90**, 316–325.

70 F. S. Taheri, A. Ghaemi, A. Maleki and S. Shahhosseini, High CO2 adsorption on amine-functionalized improved mesoporous silica nanotube as an eco-friendly nanocomposite, *Energy Fuels*, 2019, **33**(6), 5384–5397.

71 X. Wang, Q. Guo and T. Kong, Tetraethylenepentamine-modified MCM-41/silica gel with hierarchical mesoporous structure for CO2 capture, *Chem. Eng. J.*, 2015, **273**, 472–480.

72 N. A. Rashidi, S. Yusup and A. Borhan, Isotherm and thermodynamic analysis of carbon dioxide on activated carbon, *Procedia Eng.*, 2016, **148**, 630–637.

73 B. Chang, W. Shi, H. Yin, S. Zhang and B. Yang, Poplar catkin-derived self-templated synthesis of N-doped hierarchical porous carbon microtubes for effective CO2 capture, *Chem. Eng. J.*, 2019, **358**, 1507–1518.

74 M. Zhu, W. Cai, F. Verpoort and J. Zhou, Preparation of pineapple waste-derived porous carbons with enhanced CO2 capture performance by hydrothermal carbonation-alkali metal oxalates assisted thermal activation process, *Chem. Eng. Res. Des.*, 2019, **146**, 130–140.

75 S. Liu, P. Yang, L. Wang, Y. Li, Z. Wu, R. Ma, J. Wu and X. Hu, Nitrogen-doped porous carbons from lotus leaf for CO2 capture and supercapacitor electrodes, *Energy Fuels*, 2019, **33**(7), 6568–6576.

76 G. Singh, K. Ramadass, J. M. Lee, I. S. Ismail, M. Singh, V. Bansal, J.-H. Yang and A. Vinu, Convenient design of porous and heteroatom self-doped carbons for CO2 capture, *Microporous Mesoporous Mater.*, 2019, **287**, 1–8.

77 Z. Yang, G. Zhang, Y. Xu and P. Zhao, One step N-doping and activation of biomass carbon at low temperature through NaNH2: an effective approach to CO2 adsorbents, *J. CO2 Util.*, 2019, **33**, 320–329.

78 R. Wang, P. Wang, X. Yan, J. Lang, C. Peng and Q. Xue, Promising porous carbon derived from celtuce leaves with outstanding supercapacitance and CO2 capture performance, *ACS Appl. Mater. Interfaces*, 2012, **4**(11), 5800–5806.

79 D. Li, Y. Tian, L. Li, J. Li and H. Zhang, Production of highly microporous carbons with large CO2 uptakes at atmospheric pressure by KOH activation of peanut shell char, *J. Porous Mater.*, 2015, **22**(6), 1581–1588.

80 C. Ma, T. Lu, J. Shao, J. Huang, X. Hu and L. Wang, Biomass derived nitrogen and sulfur co-doped porous carbons for efficient CO2 adsorption, *Sep. Purif. Technol.*, 2022, **281**, 119899.

81 Z. Zhao, C. Ma, F. Chen, G. Xu, R. Pang, X. Qian, J. Shao and X. Hu, Water caltrop shell-derived nitrogen-doped porous carbons with high CO2 adsorption capacity, *Biomass Bioenergy*, 2021, **145**, 105969.

82 L. An, S. Liu, L. Wang, J. Wu, Z. Wu, C. Ma, Q. Yu and X. Hu, Novel nitrogen-doped porous carbons derived from graphene for effective CO2 capture, *Ind. Eng. Chem. Res.*, 2019, **58**(8), 3349–3358.

83 P. Yang, L. Rao, W. Zhu, L. Wang, R. Ma, F. Chen, G. Lin and X. Hu, Porous carbons derived from sustainable biomass via a facile one-step synthesis strategy as efficient CO2 adsorbents, *Ind. Eng. Chem. Res.*, 2020, **59**(13), 6194–6201.

84 S. Liu, L. Rao, P. Yang, X. Wang, L. Wang, R. Ma, L. Yue and X. Hu, Superior CO2 uptake on nitrogen doped carbonaceous adsorbents from commercial phenolic resin, *J. Environ. Sci.*, 2020, **93**, 109–116.

85 C. Zhang, W. Song, Q. Ma, L. Xie, X. Zhang and H. Guo, Enhancement of CO2 capture on biomass-based carbon from black locust by KOH activation and ammonia modification, *Energy Fuels*, 2016, **30**(5), 4181–4190.

86 S. W. Choi, J. Tang, V. G. Pol and K. B. Lee, Pollen-derived porous carbon by KOH activation: effect of physicochemical structure on CO2 adsorption, *J. CO2 Util.*, 2019, **29**, 146–155.